A 220–260-GHz Silicon-Micromachined Waveguide MEMS Crossover Switch

Armin Karimi, *Graduate Student Member, IEEE*, Umer Shah, *Senior Member, IEEE*,
Suxian Yu, *Student Member, IEEE*, and Joachim Oberhammer, *Senior Member, IEEE*

Abstract— This article presents a novel subterahertz (sub-THz) crossover waveguide switch concept operating in the 220–260-GHz frequency band. The crossover switching circuit is implemented by two hybrid couplers and two single-pole-single-throw (SPST) switching mechanisms, utilizing microelectromechanically reconfigurable switching surfaces. The silicon-micromachined crossover switch prototype is very compact, with a total footprint of 5.6 × 5 × 1.2 mm, including four standard WR-3.4 waveguide ports and the waveguide routing to these ports. The measured insertion loss (IL) is 0.9–1.4 dB in the crossover state and 0.8–1.3 dB in the straight state from 220 to 260 GHz, and the isolation (ISO) is better than 29.3 and 29 dB, respectively, for these states. The measured return loss (RL) is better than 14 dB in the crossover state and better than 13.6 dB in the straight state. Besides, the measured input-to-input ISO is better than 13.7 and 34 dB in the crossover and straight states, respectively. The measurement results are in excellent agreement with the simulation data. Moreover, the signal paths are fully symmetric for all input-to-output signal paths, making the crossover switching circuit suitable for redundancy applications.

Index Terms— Crossover, crossover switch, E-plane transition, hybrid-coupler, MEMS, MEMS actuator, millimeter wave, rectangular waveguide, redundancy, silicon micromachining, single-pole-double-throw (SPDT) switch, single-pole-single-throw (SPST) switch, subterahertz (sub-THz), switch, waveguide, waveguide switch.

I. INTRODUCTION

THE subterahertz (sub-THz) frequency bands have recently attracted considerable scientific and industrial attention. The short wavelength above 100 GHz leads to compact and low-weight devices, even for complex waveguide and antenna systems. Besides, the large available bandwidth at the sub-THz range makes this frequency spectrum well-suited for different applications, such as short-range car radars [1], [2], [3], [4], high-resolution imaging systems for biomedical imaging [5], [6], [7] and security screening [8], [9], high

data-rate telecommunication systems [10], [11], [12], and radio astronomy [13], [14].

As of today, computer-numerical-control (CNC) milling is still the dominant fabrication method for sub-THz systems, despite its disadvantages of fabricating bulky and heavy devices and its nonsuitability for volume manufacturing. In contrast to that, silicon micromachining, using deep-reactive-ion-etching (DRIE) and subsequent sidewall metallization, offers several improvements for fabricating devices and systems operating at the sub-THz frequency bands [15], [16], [17]. This technique offers precise fabrication of micrometer-size features and complex 3-D structures. This precision, combined with volume-manufacturing capability and high product uniformity, enables the exploitation of the sub-THz frequency spectrum on a larger scale for various applications.

Rectangular waveguides are preferred for devices operating at the sub-THz frequencies, compared to planar transmission lines, due to their low insertion loss (IL). The surface roughness is the most critical parameter affecting the IL of a rectangular waveguide at these frequencies [18]. Silicon micromachining achieves a surface roughness of a few nanometers, superior to any other fabrication techniques, leading to the lowest IL waveguides reported in the literature. For instance, WR-3.4 and WR-1.5 silicon micromachined rectangular waveguides were characterized with an IL of 0.02–0.07 and 0.05–0.07 dB/mm, respectively [15], [18]. Many silicon-micromachined components, such as single-pole-single-throw (SPST) switches [19], [20], phase shifters [21], antenna arrays [22], [23], transitions [24], and filters [25] operating at the sub-THz frequencies, are successfully demonstrated in the literature with outstanding performance.

Many applications require reconfigurable circuits, for which switches are critical for adding this reconfigurability to the systems, for instance, for frequency band selection in filter banks or radiation pattern reconfiguration in antenna arrays and radar sensors [23], [26], [27]. Conventional waveguide switches, though achieving excellent RF performance, are based on macroscale mechanics and comprise a waveguide section to be moved or rotated by a stepper motor [28], [29] and thus are bulky, heavy, slow, and have high power consumption. Besides, circuits based on such switching elements cannot achieve high integration density. For instance, although the mechanical single-pole-double-throw (SPDT) switch recently reported in [28] has excellent isolation (ISO) and IL performance, it is unsuitable for applications with
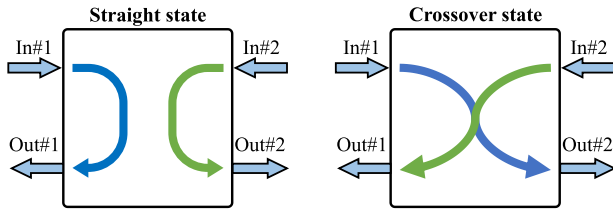
Fig. 1. Operation principle of the proposed crossover switch concept in different states.

volume manufacturing requirements, and its switching speed, size, and power consumption do not fulfill the requirements in many applications.

In contrast to macromechanical waveguide switches, microelectromechanical-based (MEMS-based) switches integrated in silicon-micromachined waveguides have the potential to outperform the existing switching technologies since they exhibit low IL, high ISO, high linearity, large operation bandwidth, low power consumption, switching speed in the microsecond range, and high degree of miniaturization. The SPST MEMS switch operating in the 500–750 GHz [19] was the first miniaturized rectangular waveguide-based switch operating at the sub-THz frequencies. Karimi et al. [20] have recently reported on an improved SPST switch concept operating in the 220–290-GHz frequency band with ISO, IL, and return loss (RL) of better than 30, 1, and 17 dB, respectively.

This article presents a novel crossover switch concept, which is a generalized symmetric switching circuit with four ports, i.e., two input and two output ports. The crossover switching mechanism is implemented by two hybrid couplers and two SPST switches controlled by MEMS comb-drive actuators. Due to its symmetric nature, leading to entirely balanced input-to-output signal paths for the different input ports, the proposed crossover switch concept can be used for redundancy switching circuits, and due to its high ISO and low IL, it can be used for receiver calibration. The concept is validated by fabricating and characterizing a crossover switch prototype operating in the 220–260-GHz frequency band, in which the measured results are in excellent agreement with the simulated data.

II. CONCEPT AND DESIGN

Fig. 1 shows the operation principle of the proposed crossover switch, which is a generalized switching circuit with two input and two output ports in different states. In the straight state (referring to Fig. 1), input ports #1 and #2 are connected directly to output ports #1 and #2, and in the crossover state, the signal paths are crossed, connecting the input ports #1 and #2 to the output ports #2 and #1. As shown in the schematic block diagram of Fig. 2(a), the proposed crossover switch concept is implemented by two hybrid couplers and two SPST switches. The signal fed to input #1 propagates through the first hybrid coupler, whose outputs are connected to two SPST switches that are operating in the same state, i.e., either both are in propagating or reflecting state. In the crossover state, the SPST switches are in
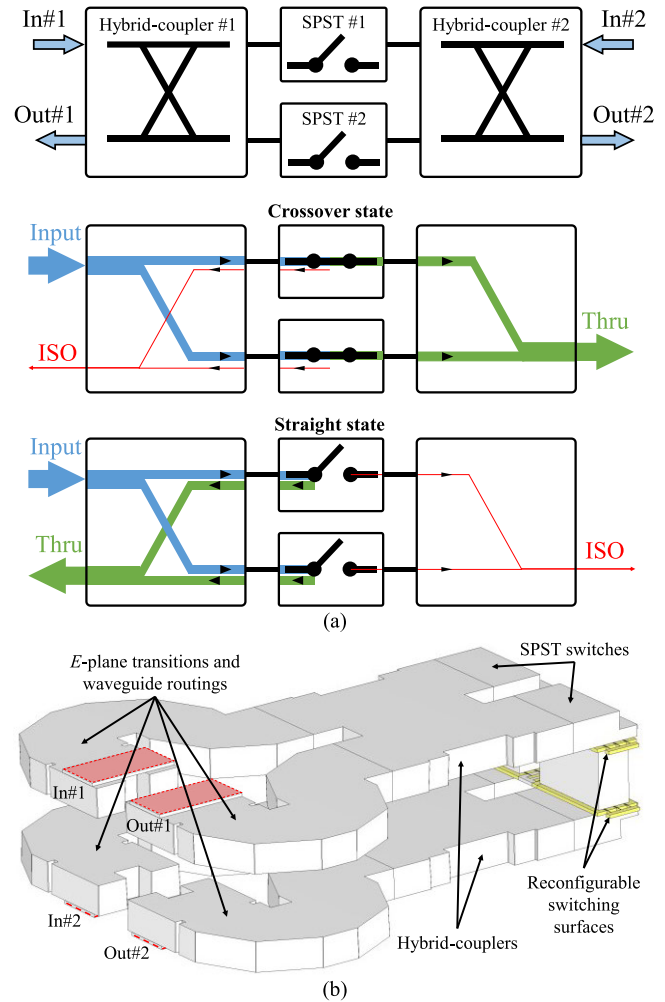

Fig. 2. (a) Schematic block diagram of the proposed crossover switch, illustrating the thru (green) and isolated (red) ports' signal path in the crossover and straight states. (b) Perspective view of the crossover switch implementation, including the hybrid couplers and SPST switches connected to four E-plane transitions to standard WR-3.4 waveguide.

the propagating state, and the −3-dB signals propagate through both SPST switches and combine in the second hybrid coupler at output #2 since the 90° phase difference between the output ports of the first coupler is compensated by the same phase difference in the second coupler. In the straight state, the SPST switches are in the reflecting state and block the signal paths between the two couplers. Thus, the reflected signals from the SPST switches are then recombined at output #1. Besides, as can be seen from the block diagram, the proposed crossover switching concept is fully symmetric regarding the input-to-output signal paths, i.e., the input #1 to output #1 or to output #2 paths are symmetric to the input #2 to output #2 or to output #1 paths, respectively.

Fig. 2(b) shows a perspective view of the micromachined waveguide implementation of the crossover switch. The couplers are implemented by multistep hybrid couplers, and the SPST switches are implemented by two sequential microelectromechanically reconfigurable switching surfaces (MEMS-RSs) [20]. There are two reasons for having two sequential MEMS-RSs in each SPST switch.
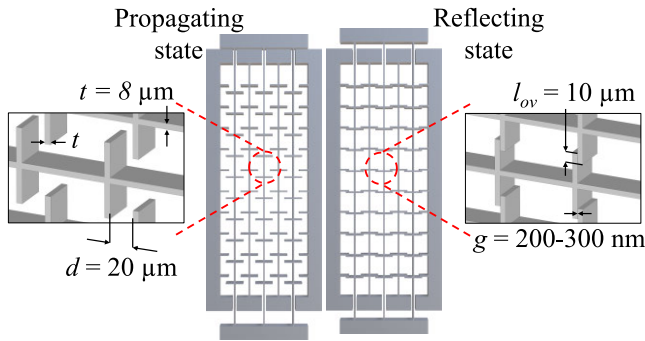
Fig. 3. Overview of the MEMS-RSs in the propagating and reflecting states with detailed dimensions (d: distance between the switching cantilevers in the propagating state, g: gap between the switching cantilevers in the reflecting state, t: thickness of the switching cantilevers, and l_{ov}: vertical overlap between the switching cantilevers).

1) In the propagating state (referring top Fig. 3), the RL of the SPST switches is minimized by two sequential MEMS-RSs in the waveguide path, which are designed for destructive interference for the reflection signals in the frequency band of interest [20]. Any reflected power from the MEMS-RSs in the propagating state is problematic for the crossover switching circuit as the reflected power recombines in the unwanted output port (the isolated port), thus degrading the ISO.

2) In the reflecting state (referring top Fig. 3), the two sequential MEMS-RSs increase the ISO of the SPST switch without impacting the IL [20]. Thus, utilizing two sequential MEMS-RSs improves the ISO of the switch as any leaked power combines in the unwanted output port (the isolated port).

Fig. 3 shows the MEMS-RSs in the propagating and reflecting states. Each MEMS-RS consists of two sets of switching cantilevers. The first set is fixed, and the second set is suspended and controlled by a comb-drive MEMS actuator. In the propagating state, there is a 20-μm distance between the fixed and suspended cantilevers, allowing the wave to propagate through the MEMS-RSs with minimal interference, as the cantilevers are significantly shorter compared to the wavelength. In the reflecting state, the cantilevers are in contact, short-circuiting the E-field of the rectangular waveguide's dominant mode (TE$_{10}$) and thus effectively reflecting the signal. According to a comprehensive study performed in [19], a large number of E-plane cantilevers increase the reflecting-state ISO but negatively influence the propagating-state RL and IL. Furthermore, a large number of H-plane cantilevers lead to better propagating-state RL and IL and deteriorate the reflecting-state ISO. Considering this tradeoff, the MEMS-RSs are designed with five E-plane and ten H-plane switching cantilever rows, resulting in 60 contact points in the reflecting state [20].

The crossover switch prototype is designed to be implemented in four vertically stacked silicon-on-insulator (SOI) chips composed of a handle, device, and buried-oxide layer thickness of 275, 30, and 3 μm, respectively. The in-plane waveguides, referring to the chip surface, are etched in the handle layers; thus, they are slightly shallower compared
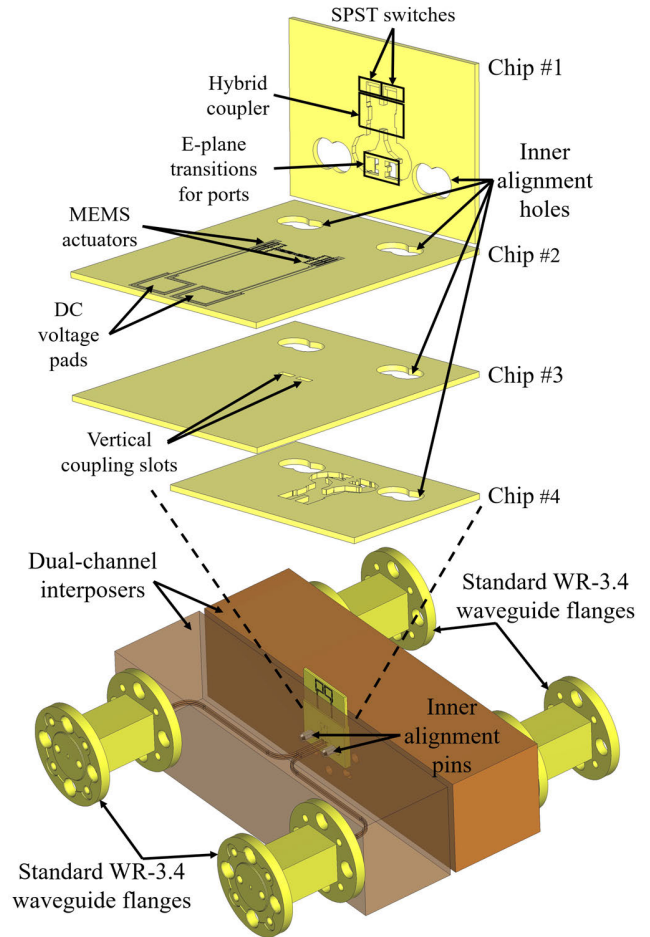

Fig. 4. Exploded view of the vertically stacked SOI chips of the crossover switch prototype and a concept view of the measurement setup showing the assembled device mounted and aligned to two custom-made interposers with inner alignment pins.

to the standard WR-3.4 waveguide height of 432 μm. The MEMS-RSs and comb-drive actuators for their operation are etched in the device layer. Furthermore, the designed crossover switch needs 12 H-plane bends for signal routing and four additional E-plane transitions at the input–output ports that facilitate direct connection of the reduced-height in-plane waveguides (849 $\times$ 275 μm) to standard-sized (864 $\times$ 432 μm) out-of-plane WR-3.4 interfaces. Fig. 4 shows an exploded view of the individual chips composing the crossover switch prototype and the concept of the assembled device mounted between two custom-made dual-channel WR-3.4 waveguide interposers. The distance between the adjacent channels of the interposer, which is made of brass and fabricated by CNC milling, is 550 μm on one side and diverted away on the opposite side to be able to connect it to two waveguide flanges in the measurement setup. As can be seen, chips #1 and #4 contain the waveguiding structures, including the hybrid couplers, waveguides of the SPST switches, and routing to the standard WR-3.4 interfaces, and chips #2 and #3 contain the MEMS-RSs, comb-drive actuators, and vertical coupling slots.
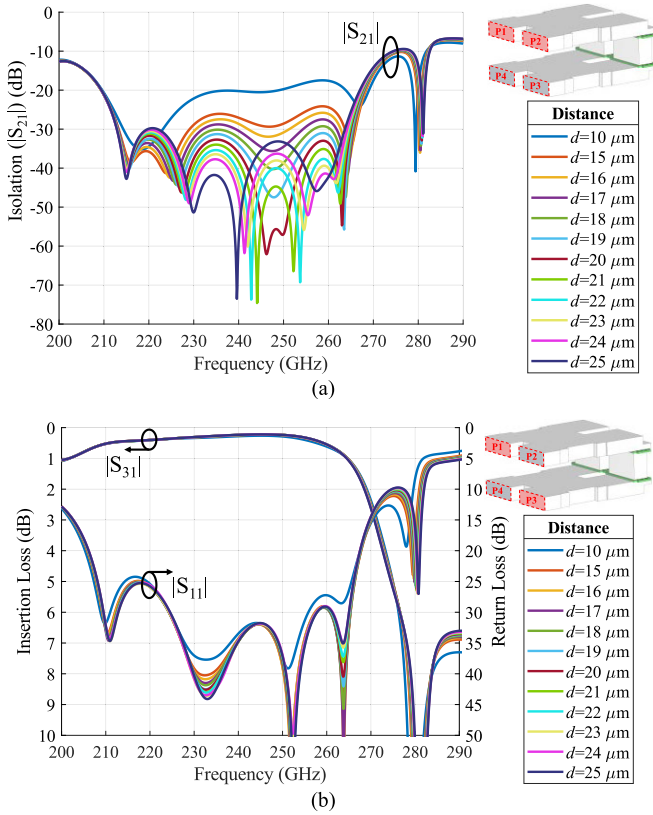
Fig. 5. Simulated performance of the designed crossover switch, without the *E*-plane transitions and waveguide routings, with different distances between the switching cantilevers (*d*: referring to Fig. 3) in the crossover state. (a) ISO. (b) IL and RL.

Fig. 6. Simulated performance of the designed crossover switch, without the *E*-plane transitions and waveguide routings, with different gaps between the switching cantilevers (*g*: referring to Fig. 3) in the straight state. (a) ISO. (b) IL and RL.

The subcomponents of the designed switch prototype are optimized separately before fine-tuning the overall device, and all the full-wave simulations are performed by CST Microwave Studio Suits. Besides, according to the frequency band requirements outlined in the CAR2TERA project, 238–248-GHz band, the crossover switching circuit is designed to operate properly within a broader bandwidth of 220–260 GHz to ensure optimal performance and robustness of the switching circuit. Fig. 5(a) and (b) shows the simulated performance of the crossover switch, without the *E*-plane transitions and waveguide routings, for different switching cantilever distances (*d*: referring to Fig. 3) in the crossover state. The simulated crossover-state ISO, IL, and RL are better than 32, 0.3–0.6, and 26 dB, respectively, between 220 and 260 GHz for a cantilever distance of 20 μm. Moreover, Fig. 6(a) and (b) shows the simulated performance of the crossover switch, without the *E*-plane transitions and waveguide routings, for different contact gaps (*g*: referring to Fig. 3) in the straight state. The switching mechanism is designed to be robust against variations in the contact gap and achieves its performance even when the switching cantilevers are not in full contact but in capacitive mode with a contact gap of up to 250 nm. The ISO, IL, and RL are better than 32, 0.2–0.5, and 12.5 dB, respectively, from 220 to 260 GHz for a contact gap of 250 nm.
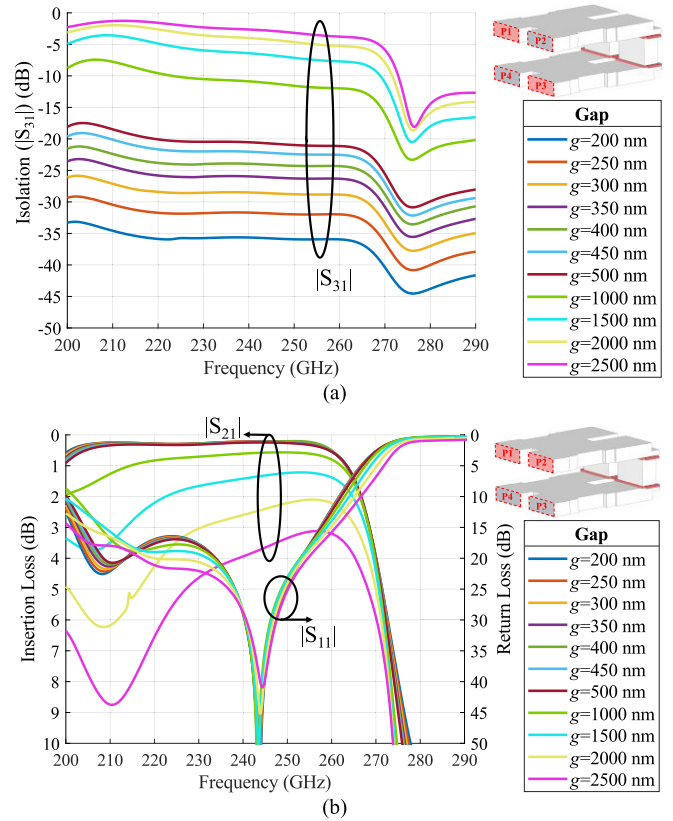
A. Hybrid Coupler

Fig. 7(a) shows an overview of the designed multistep hybrid coupler utilized to implement the crossover switch, with detailed dimensions. The coupler is optimized for having high ISO, low RL, amplitude balanced, and 90° out-of-phase outputs in the design bandwidth of 220–260 GHz. According to Fig. 7(c), which shows the simulated performance of the hybrid coupler, the RL and ISO are better than 30 dB, and the output phase error is better than 1° from 220 to 260 GHz. As can be seen, the amplitude of the output ports is not entirely balanced for the whole frequency range, i.e., there is a slight difference between the coupled and thru ports, which is typical for such a multistep coupler geometry.

B. SPST Switch

The SPST switches are the core components in the proposed crossover switch concept. The complete design procedure of the utilized SPST switches, which are based on two MEMS-RSs that are positioned sequentially in the signal path in order to improve the ISO, as well as the IL and RL, has previously been published by Karimi et al. [20]. Fig. 7(b) shows a perspective view of the SPST switch with detailed dimensions, and Fig. 7(d) shows the simulated performance for a 20-μm distance between the switching cantilevers in the propagating state and a 250-nm contact gap in the reflecting state.
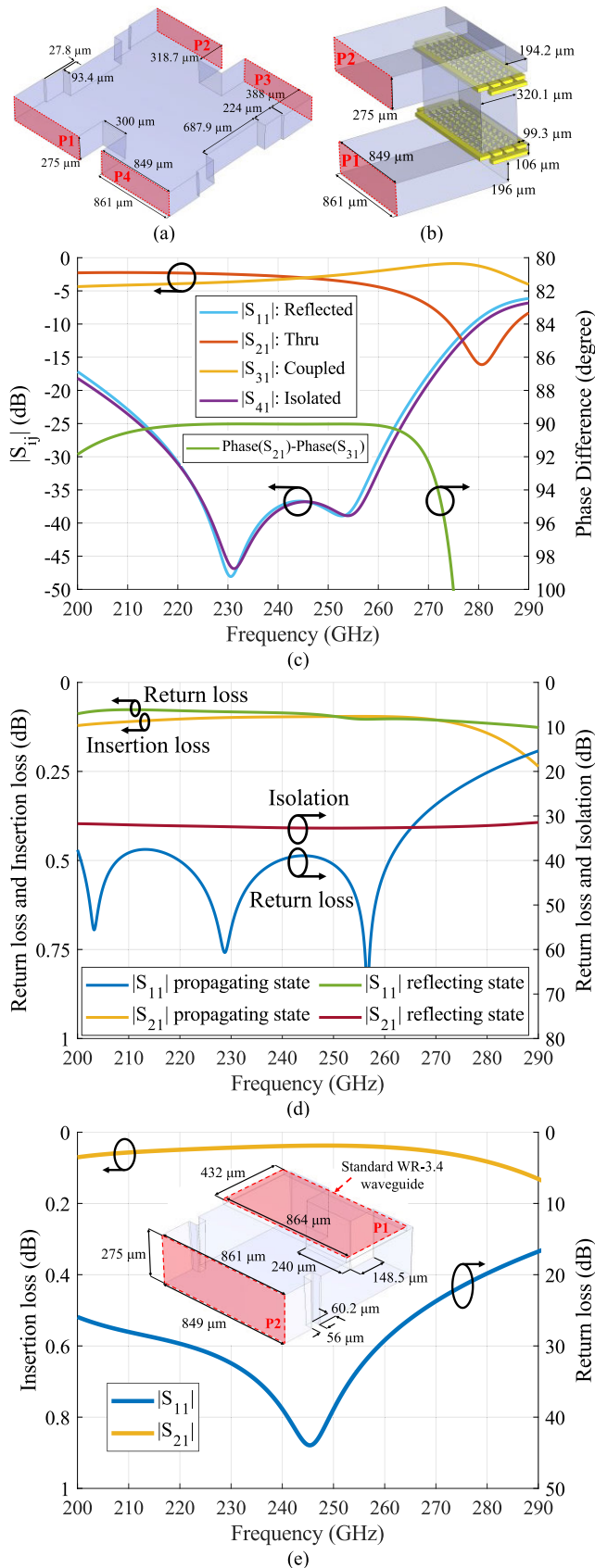
Fig. 7. Perspective view and detailed dimensions of the designed. (a) Multi-step hybrid coupler and (b) SPST switch. Simulated performance of (c) hybrid coupler and (d) SPST switch. (e) Simulated performance of the *E*-plane transition, utilized for the input–output ports, along with its perspective view and detailed dimensions.
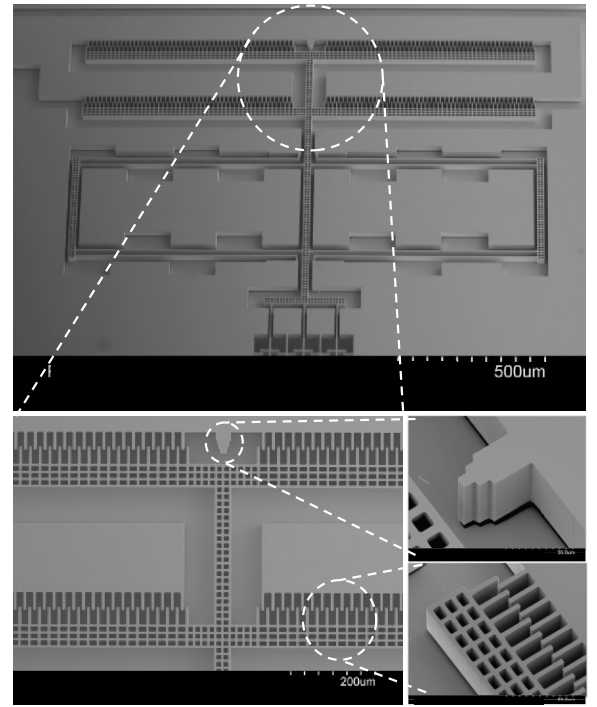

Fig. 8. SEM image of the microelectromechanical comb-drive actuator with zoomed-in view of the stopping mechanism and interdigitated comb fingers.

C. E-Plane Transition

An overview of the *E*-plane transition, utilized for the input–output waveguide port interfaces, is shown in Fig. 7(e), along with its detailed dimensions [24]. According to Fig. 7(e), the simulated insertion and return losses are better than 0.1 and 20 dB between 200 and 280 GHz, respectively.

D. Electrostatic Actuator

The actuation mechanism consists of four comb-drive push–pull actuator sections on each side of the MEMS-RSs, in which every section consists of 50 interdigitated comb fingers. Besides, the restoring mechanism consists of eight parallel 1.5-folded beam mechanical springs, also placed on both sides of the MEMS-RSs. The push–pull actuator is designed to displace the MEMS-RSs by ± 10 μm at a nominal actuation voltage of 40 V. Fig. 8 shows a scanning electron microscope (SEM) image of the actuating system with zoomed-in views of the stopping mechanism and interdigitated comb fingers. Moreover, the natural resonance frequency of the mass-spring system, which defines an upper bound for the switching speed, is calculated numerically and is around 2.1 KHz. Thus, the switching speed is expected to be in the order of a few hundred microseconds.

III. FABRICATION AND ASSEMBLY

The designed crossover switch prototype consists of four vertically stacked SOI chips. Three masks for the handle layer and one mask for the device layer are used to etch different features on the SOI wafer. Starting from a thermally oxidized SOI wafer, the device layer and the first handle layer mask
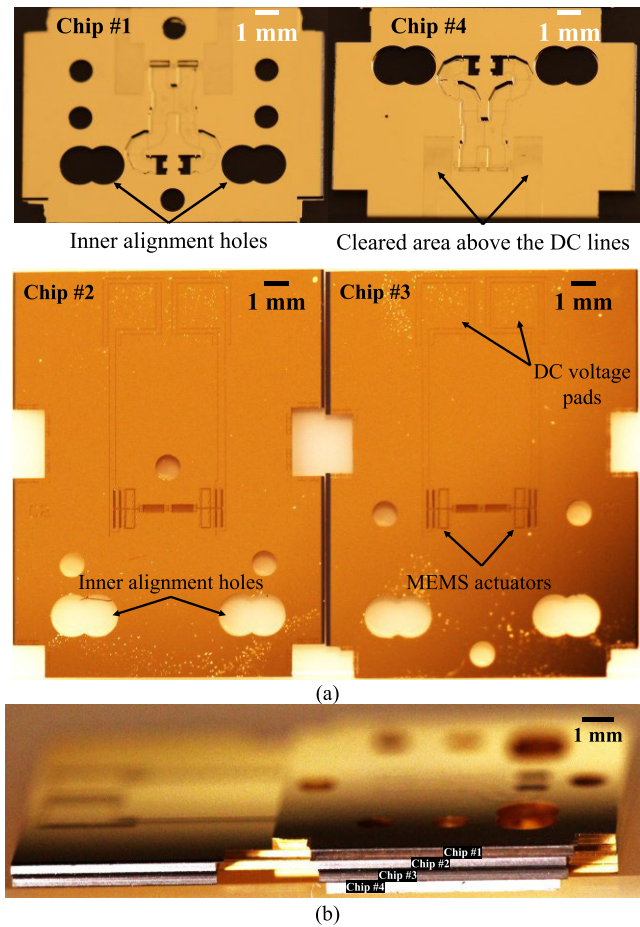
(a)

(b)

Fig. 9. Photograph of the fabricated chips (a) before and (b) after the thermocompression bonding. As can be seen in (b), the top and the bottom chips (chips #1 and #4) are smaller compared to the middle ones (chips #2 and #3), facilitating access to the dc voltage pads.

patterns are transferred on the wafer by photolithography and dry etching of the thermal oxide layers. The first handle layer mask includes clearance areas above the dc voltage lines and the moving parts to avoid short-circuiting and to enable a free movement of the mechanical parts. Next, 150 nm of amorphous silicon is deposited on the wafer as an etch-stop layer. Then, a further 1.5-μm-thick silicon dioxide layer is deposited on the handle layer as the second handle layer mask, with plasma-enhanced-chemical-vapor-deposition (PECVD) and patterned by photolithography and oxide dry etching. The second handle layer mask is used for etching the steps inside the waveguides. The same process is repeated for the third handle layer mask, which is for etching the full-height waveguides. After transferring all the mask patterns onto the silicon dioxide layers on both sides of the wafer, first, the handle layer and then the device layer are etched by DRIE process. Afterward, the moving parts are released by vapor hydrofluoric acid (HF). Next, the chips are metalized with 200 and 1000 nm of gold on the device and handle layers, respectively. Finally, the metalized chips are bonded by thermocompression bonding at 200 °C.

Fig. 9(a) and (b) shows the photographs of the fabricated chips before and after bonding. As can be seen, for accessing

the dc voltage pads, the top and bottom chips (chips #1 and #4) are smaller compared to the middle ones (chips #2 and #3). Moreover, Fig. 10 shows the four SEM images of the fabricated chips. Fig. 10(a) shows a top view of the chips containing the waveguide structures (chips #1 and #4); Fig. 10(b) shows a zoomed-in view of the switching junction, in which the E-plane step and the clearance above the dc lines and moving parts can be seen clearly, and the debris visible in the cross section view AA′ is due to the dicing process. Fig. 10(c) shows the H-plane bends and the E-plane transitions to standard WR-3.4 waveguide ports; Fig. 10(d) shows a top view of the MEMS actuators and MEMS-RSs with a close-up view of the switching cantilevers on chips #2 and #3.

IV. Characterization and Analysis

The RF performance of the fabricated crossover switch prototype is measured by a Rohde & Schwarz ZVA-24 VNA with ZC330 frequency extenders, calibrated by a standard calibration kit with thru-offset-short-match (TOSM) method. Fig. 11(a) shows the assembled device mounted between the two interposers and aligned to them by inner alignment pins. One of the inner alignment holes on the fabricated device is tightly fit with a circular hole, and the other is a loose elliptical hole, ensuring a repeatable alignment precision of ±5 μm [25], [30]. The overall structure, which is fixed on a custom-made holder [shown in Fig. 11(a)], has four standard WR-3.4 interfaces, in which the unwanted ports are loaded by sub-THz match loads in every measurement to reduce the effect of the reflected power from other ports. Moreover, Fig. 11(b) and (c) shows the configuration of the measurement setup, where the interposers are connected to the frequency extenders in the measurement setup, and the switch is actuated with five micrometer-size needles, which are fixed on precise dc probe positioners. Fig. 11(b) depicts the measurement setup for measuring input #1 to output #2 (referring to Fig. 2), and Fig. 11(c) shows the measurement setup for measuring input #1 to input #2 (referring to Fig. 2).

After all the flange-to-flange measurements, which include the interposers and the crossover switch sandwiched between them, the S-parameters of the interposers are measured and de-embedded from the measured flange-to-flange results by postprocessing the data in MATLAB. Thus, the reference (calibration) planes are shifted to the surface of the crossover switch device [referring to Fig. 2(b)].

Fig. 12(a) and (b) shows the measured and simulated input-to-output ($|S_{21}|$ in the crossover state and $|S_{31}|$ in the straight state) and input-to-input ($|S_{41}|$) ISOs of the fabricated crossover switch prototype in the crossover and straight states, respectively. The applied actuation voltage is 44 V in the crossover state and 50 V in the straight state. The measured input-to-output ISOs in the crossover and straight states are better than 29.3 and 29 dB in the 220–260-GHz frequency band, respectively, and are in excellent agreement with the simulation data. Besides, as expected from the simulation data, the input-to-output ISO in the straight state remains uniform across the operating band, and by comparing the measured performance with the simulation data, it can be inferred that
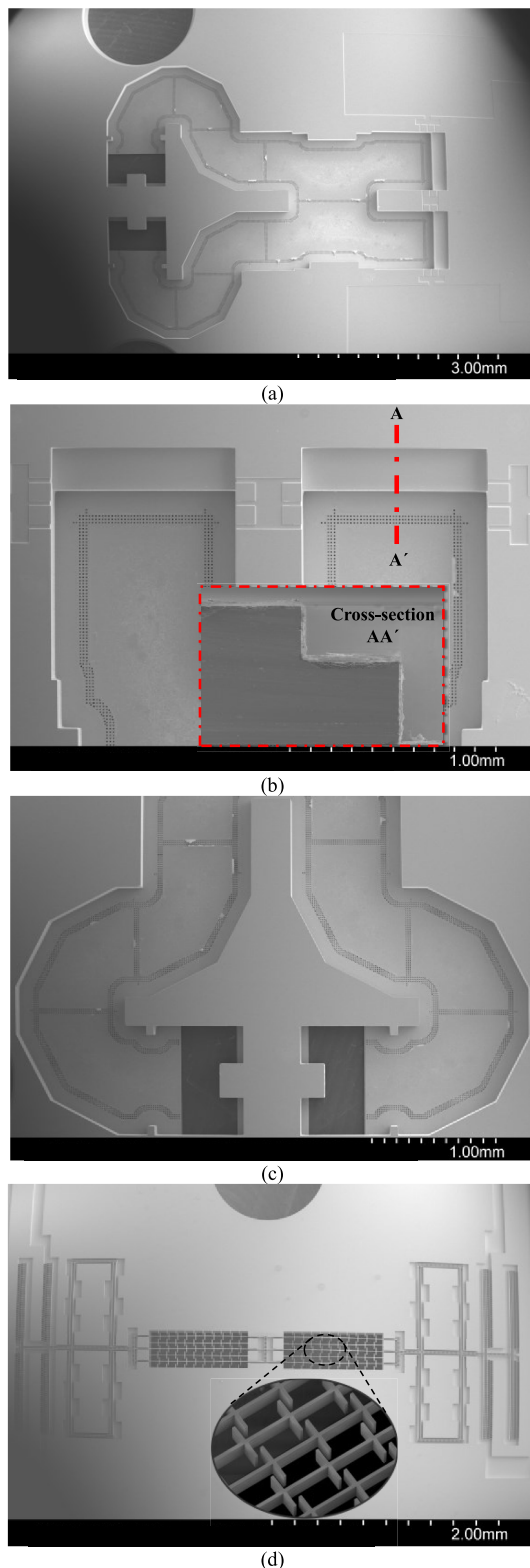
Fig. 10.   SEM images of the fabricated chips after metallization. (a) Top view of the waveguide structures. (b) Overview of the switching junction and a cross section view AA′ of a diced chip. (c) Overview of the H-plan bends and E-plane transitions to standard WR-3.4 waveguide interfaces. (d) Top view of the MEMS actuators and MEMS-RSs, and a zoomed-in view of the switching cantilevers.

Fig. 11.   (a) Assembled crossover switch prototype mounted between two interposers and fixed on a custom-made holder with screws, along with an illustration of the device aligned to an interposer with inner alignment pins. Configuration of the measurement setup for measuring (b) input #1 to output #2 (referring to Fig. 2) and (c) input #1 to input #2 (referring to Fig. 2).

the contact gap is between 250 and 300 nm in the straight state at the actuation voltage of 50 V. Furthermore, according to Fig. 12(a) and (b), the input-to-input ISOs are better than
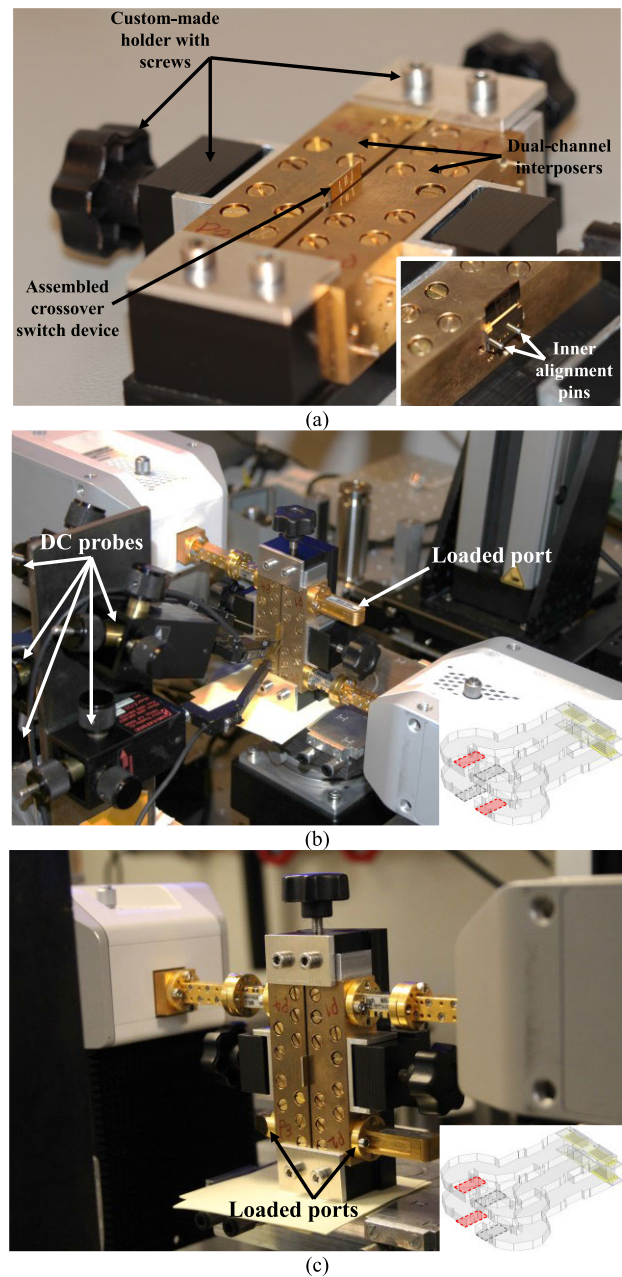
13.7 and 34 dB from 220 to 260 GHz in the crossover and straight states, respectively.

Fig. 13(a) and (b) shows the measured and simulated IL in the crossover and straight states, respectively ($|S_{31}|$ in the crossover state and $|S_{21}|$ in the straight state). The crossover-state IL is between 0.9 and 1.4 dB in the 220–260-GHz frequency band at the actuation voltage of 44 V. According to the inset in Fig. 13(a), the crossover-state IL does not change considerably by displacing the reconfigurable switching surfaces from the nonactuated state to the full-actuated state, which was expected according to the simulation data shown in Fig. 5(b). On the contrary, as can be seen
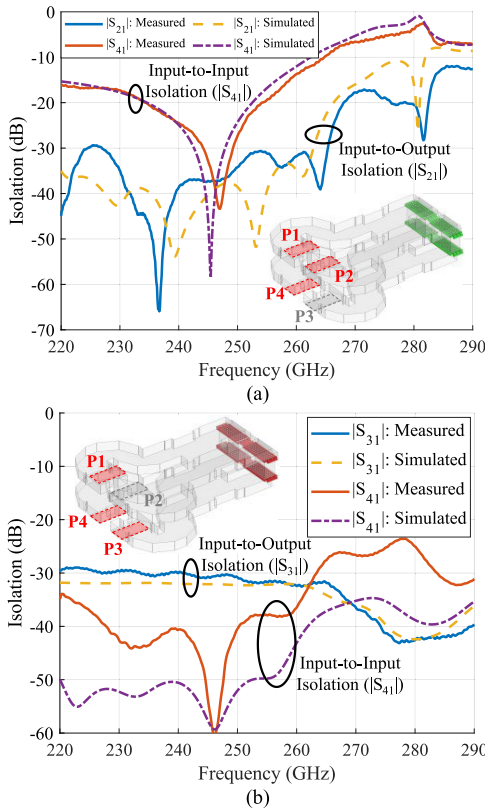
Fig. 12. Measured and simulated input-to-output and input-to-input ISOs of the crossover switch in (a) crossover and (b) straight states.
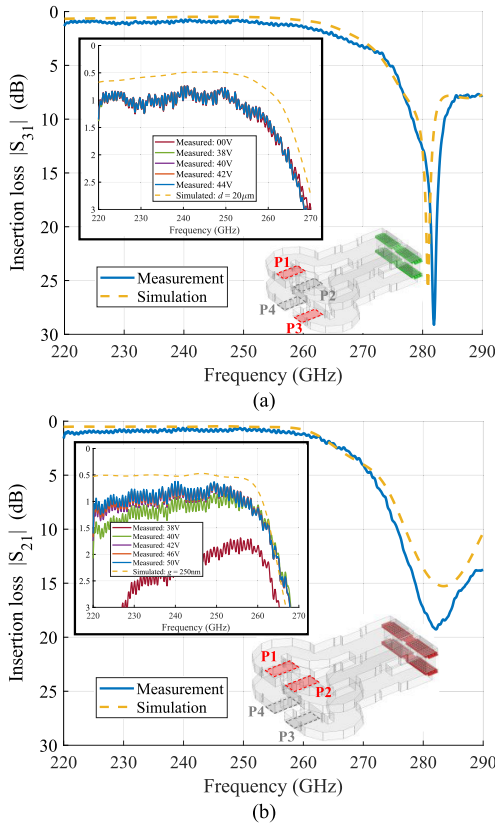

Fig. 13. Measured and simulated IL of the crossover switch in (a) crossover and (b) straight states.
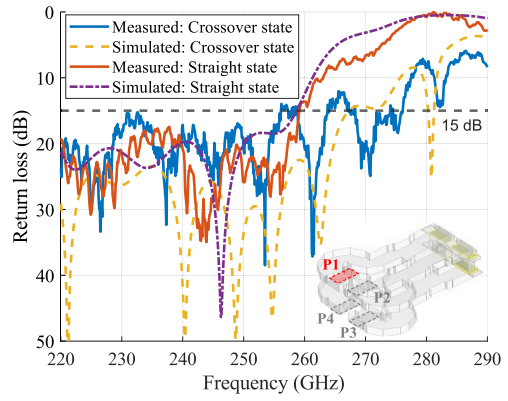

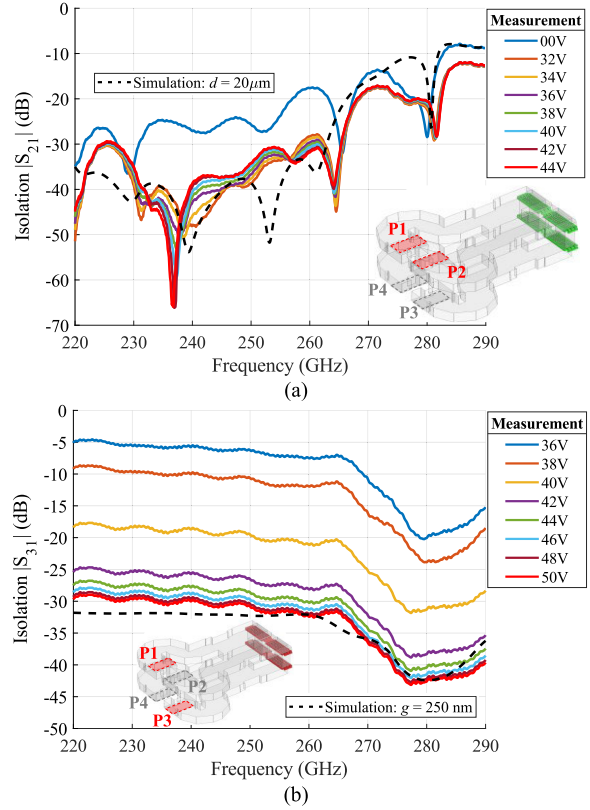Fig. 14. Measured and simulated RL of the crossover switch in the crossover and straight states.

Fig. 15. Measured and simulated input-to-output ISO of the crossover switch at different actuation voltages in (a) crossover and (b) straight states.

between 220 and 260 GHz at the actuation voltage of 50 V, which is in excellent agreement with the simulation data shown in Fig. 6(b). Furthermore, Fig. 14 shows the measured and simulated RL of the crossover switch in the crossover and straight states. According to Fig. 14, the RL is better than 14 and 13.6 dB from 220 to 260 GHz for the crossover and straight states, respectively, and is better than 15 dB for more than 95% of the bandwidth. After analyzing the measured results, it can be concluded that the fabricated crossover switch prototype achieves an excellent performance from 220 to 260 GHz, 16.6% fractional bandwidth, with excellent agreement between the measured results and the simulated data.

According to the simulations shown in Figs. 5(a) and 6(a), the input-to-output ISOs ($|S_{21}|$ in the crossover state and $|S_{31}|$ in the straight state) are changing significantly by changing the

from the inset in Fig. 13(b), the straight-state IL depends strongly on the contact gap and is better than 0.8–1.3 dB

TABLE I

COMPARISON OF THE PRESENTED CROSSOVER SWITCH WITH OTHER STATE-OF-THE-ART MM-WAVE AND SUB-THZ WAVEGUIDE SWITCHES. FOR COMPARISON, THREE STATE-OF-THE-ART SOLID-STATE SEMICONDUCTOR-BASED SWITCHES ARE ALSO ADDED AT THE BOTTOM OF THE TABLE

Ref	Switch type	Frequency range (FBW)	Technology	Isolation (dB)	IL (dB)	RL (dB)
[31]	SPST	60-70 GHz (15.4 %)	Silicon micromachined MEMS waveguide switch	> 30	< 0.65	> 15
[32]	SPST	60-75 GHz (22.2 %)	Monolithic millimeter-wave MEMS waveguide switch	> 22	< 0.2	> 12.5
[20]	SPST	220-290 GHz (27.4 %)	Silicon micromachined MEMS waveguide switch	28.5-32.5	0.7-1.2	> 17
[33]	SPST	240-320 GHz (28.5 %)	Silicon micromachined shunt capacitor MEMS switch embedded in a CNC-milled waveguide	> 16	< 2	> 16
[28]	SPDT	250-310 GHz (21.4 %)	Piezo-motor actuated CNC-milled waveguide switch	> 75	< 0.6	> 20
[34]	SPST	360-500 GHz (32.5 %)	Silicon micromachined MEMS waveguide switch embedded in a CNC-milled waveguide	> 25	< 6	> 6
[35]	SPDT	420-500 GHz (17 %)	Silicon micromachined MEMS waveguide switch embedded in a CNC-milled waveguide	> 23	< 1	> 23
[36]	SPST	500-750 GHz (40 %)	Silicon micromachined MEMS waveguide switch embedded in a CNC-milled waveguide	> 20	< 3	> 20
[19]	SPST	500-750 GHz (40 %)	Silicon micromachined MEMS waveguide switch	19-24	2.5-3	6-8
[37]	SPDT	500-750 GHz (40 %)	Silicon micromachined MEMS rotating switch	> 20	< 3	Not mentioned
[38]	SPST	500-750 GHz (40 %)	RF-MEMS DC contact switch	> 17	0.7-2.7	> 12
This work	**Crossover**	**220-260 GHz (16.6 %)**	**Silicon micromachined MEMS waveguide switch**	**> 29**	**< 1.4**	**> 13.6**
[39]	SPDT	75-110 GHz (37.8 %)	90-nm CMOS	> 40	2.6-3.4	> 10
[40]	SPDT	130-180 GHz (32.2 %)	65-nm bulk CMOS	21.1-23.7	3.3-4	> 10
[41]	SPDT	140-220 GHz (44.4 %)	45-nm CMOS SOI	20-30	3-4.5	> 10

distance between the switching cantilevers, d in the crossover state, and g in the straight state (referring to Fig. 3). Thus, the input-to-output ISOs are measured at different actuation voltages, which are corresponding to different distances between the switching cantilevers and shown in Fig. 15(a) and (b). Furthermore, the performance of the fabricated crossover switch prototype is summarized and compared to other state-of-the-art mm-wave and sub-THz switches in Table I. According to Table I, the presented crossover switch outperforms all the other switches except for the macromechanical SPDT switch presented in [28] by JPL. Compared to the latter switch, the presented crossover switch in this article, though having lower ISO and slightly higher IL, is three orders of magnitude compacter, has near-zero power consumption, and is faster by at least three orders of magnitude due to its electrostatic MEMS actuator nature. Besides, the presented crossover switch with two input and two output ports is a generalized form of SPDT switches and has more advanced circuit functions compared to SPDT switches, i.e., loading either input port #1 or #2 [referring to Fig. 2(b)] transforms the crossover switch into an SPDT switch with a single input and double outputs.

V. CONCLUSION

A novel crossover switch, consisting of two hybrid couplers and two SPST switches, is successfully demonstrated in this article. The proposed crossover switch concept is validated by a switch prototype operating in the 220–260-GHz frequency band, with excellent agreement between the measured results and the simulated data. In essence, the function of the proposed switch can be explained as a switchable resonance circuit composed of a resonating section between two MEMS-RSs. Based on this principle, it is possible to compose more complex elements in the circuit, for instance, for achieving larger bandwidth by adding more of such sections and MEMS-RSs. The prototype is fabricated by silicon micromachining and implemented with four vertically stacked SOI chips. The switching is performed by two microelectromechanically reconfigurable switching surfaces, which are controlled by two microelectromechanical comb-drive actuators. Due to the symmetry of the design, the presented switch is well-suited for applications with redundancy requirements. Besides, it can be used for receiver calibration due to excellent ISO, IL, and RL performance with the measured ISO/IL/RL of better than 29.3/0.9–1.4/14 dB and 29/0.8–1.3/13.6 dB for the fabricated prototype in the crossover and straight states, respectively. The novelty and excellent performance of the proposed crossover switch make it a significant progress toward developing more sophisticated switching circuits.

REFERENCES

[1] Z. Liu et al., "Robust target recognition and tracking of self-driving cars with radar and camera information fusion under severe weather conditions," *IEEE Trans. Intell. Transp. Syst.*, vol. 23, no. 7, pp. 6640–6653, Jul. 2022, doi: 10.1109/TITS.2021.3059674.

[2] M. Moallem and K. Sarabandi, "Polarimetric study of MMW imaging radars for indoor navigation and mapping," *IEEE Trans. Antennas Propag.*, vol. 62, no. 1, pp. 500–504, Jan. 2014, doi: 10.1109/TAP.2013.2289354.

[3] K.-Y. Guo, E. G. Hoare, D. Jasteh, X.-Q. Sheng, and M. Gashinova, "Road edge recognition using the stripe Hough transform from millimeter-wave radar images," *IEEE Trans. Intell. Transp. Syst.*, vol. 16, no. 2, pp. 825–833, Apr. 2015, doi: 10.1109/TITS.2014.2342875.

[4] J. A. Zhang, X. Huang, Y. J. Guo, J. Yuan, and R. W. Heath, "Multibeam for joint communication and radar sensing using steerable analog antenna arrays," *IEEE Trans. Veh. Technol.*, vol. 68, no. 1, pp. 671–685, Jan. 2019, doi: 10.1109/TVT.2018.2883796.

[5] T. C. Bowman, M. El-Shenawee, and L. K. Campbell, "Terahertz imaging of excised breast tumor tissue on paraffin sections," *IEEE Trans. Antennas Propag.*, vol. 63, no. 5, pp. 2088–2097, May 2015, doi: 10.1109/TAP.2015.2406893.

[6] J. B. Baxter and G. W. Guglietta, "Terahertz spectroscopy," *Anal. Chem.*, vol. 83, no. 12, pp. 4342–4368, Jun. 2011, doi: 10.1021/ac200907z.

[7] K. Ajito and Y. Ueno, "THz chemical imaging for biological applications," *IEEE Trans. THz Sci. Technol.*, vol. 1, no. 1, pp. 293–300, Sep. 2011, doi: 10.1109/TTHZ.2011.2159562.

[8] K. B. Cooper et al., "Penetrating 3-D imaging at 4- and 25-m range using a submillimeter-wave radar," *IEEE Trans. Microw. Theory Techn.*, vol. 56, no. 12, pp. 2771–2778, Dec. 2008, doi: 10.1109/TMTT.2008.2007081.

[9] K. B. Cooper, R. J. Dengler, N. Llombart, B. Thomas, G. Chattopadhyay, and P. H. Siegel, "THz imaging radar for standoff personnel screening," *IEEE Trans. THz Sci. Technol.*, vol. 1, no. 1, pp. 169–182, Sep. 2011, doi: 10.1109/TTHZ.2011.2159556.

[10] P. Hillger, J. Grzyb, R. Jain, and U. R. Pfeiffer, "Terahertz imaging and sensing applications with silicon-based technologies," *IEEE Trans. THz Sci. Technol.*, vol. 9, no. 1, pp. 1–19, Jan. 2019, doi: 10.1109/TTHZ.2018.2884852.

[11] H. Sarieddeen, M.-S. Alouini, and T. Y. Al-Naffouri, "An overview of signal processing techniques for terahertz communications," *Proc. IEEE*, vol. 109, no. 10, pp. 1628–1665, Oct. 2021, doi: 10.1109/JPROC.2021.3100811.

[12] T. S. Rappaport et al., "Wireless communications and applications above 100 GHz: Opportunities and challenges for 6G and beyond," *IEEE Access*, vol. 7, pp. 78729–78757, 2019, doi: 10.1109/ACCESS.2019.2921522.

[13] K. Rudakov et al., "Low-noise THz-range Nb based SIS receivers for radio astronomy," in *Proc. 45th Int. Conf. Infr., Millim., THz Waves (IRMMW-THz)*, Nov. 2020, pp. 1–2, doi: 10.1109/IRMMW-THz46771.2020.9370465.

[14] P. Moseley, G. Savini, and P. Ade, "Large aperture metal-mesh lenses for THz astronomy," in *Proc. 12th Eur. Conf. Antennas Propag. (EuCAP)*, Apr. 2018, pp. 1–3, doi: 10.1049/cp.2018.0604.

[15] C. Jung-Kubiak et al., "A multistep DRIE process for complex terahertz waveguide components," *IEEE Trans. THz Sci. Technol.*, vol. 6, no. 5, pp. 690–695, Sep. 2016, doi: 10.1109/TTHZ.2016.2593793.

[16] G. Chattopadhyay, J. S. Ward, H. Manohara, and R. Toda, "Deep reactive ion etching based silicon micromachined components at terahertz frequencies for space applications," in *Proc. 33rd Int. Conf. Infr., Millim. THz Waves*, Sep. 2008, pp. 5–6, doi: 10.1109/icimw.2008.4665514.

[17] T. J. Reck, C. Jung-Kubiak, J. Gill, and G. Chattopadhyay, "Measurement of silicon micromachined waveguide components at 500–750 GHz," *IEEE Trans. THz Sci. Technol.*, vol. 4, no. 1, pp. 33–38, Jan. 2014, doi: 10.1109/TTHZ.2013.2282534.

[18] B. Beuerle, J. Campion, U. Shah, and J. Oberhammer, "A very low loss 220–325 GHz silicon micromachined waveguide technology," *IEEE Trans. THz Sci. Technol.*, vol. 8, no. 2, pp. 248–250, Mar. 2018, doi: 10.1109/TTHZ.2018.2791841.

[19] U. Shah et al., "A 500–750 GHz RF MEMS waveguide switch," *IEEE Trans. THz Sci. Technol.*, vol. 7, no. 3, pp. 326–334, May 2017, doi: 10.1109/TTHZ.2017.2670259.

[20] A. Karimi, U. Shah, and J. Oberhammer, "Compact high-isolation sub-THz micro-electromechanical SPST switch," in *Proc. 53rd Eur. Microw. Conf. (EuMC)*, Sep. 2023, pp. 452–455, doi: 10.23919/eumc58039.2023.10290353.

[21] X. Zhao, U. Shah, O. Glubokov, and J. Oberhammer, "Micromachined subterahertz waveguide-integrated phase shifter utilizing supermode propagation," *IEEE Trans. Microw. Theory Techn.*, vol. 69, no. 7, pp. 3219–3227, Jul. 2021, doi: 10.1109/TMTT.2021.3076079.

[22] A. Gomez-Torrent et al., "A 38 dB gain, low-loss, flat array antenna for 320–400 GHz enabled by silicon-on-insulator micromachining," *IEEE Trans. Antennas Propag.*, vol. 68, no. 6, pp. 4450–4458, Jun. 2020, doi: 10.1109/TAP.2020.2969753.

[23] A. Karimi, U. Shah, and J. Oberhammer, "Sub-THz silicon-micromachined reconfigurable beam-steering frontend," in *Proc. 53rd Eur. Microw. Conf. (EuMC)*, Sep. 2023, pp. 448–451, doi: 10.23919/eumc58039.2023.10290347.

[24] A. Karimi, M. M. Gohari, O. Glubokov, U. Shah, and J. Oberhammer, "Full-band silicon-micromachined E-plane waveguide bend for flange-to-chip connection," *IEEE Trans. THz Sci. Technol.*, vol. 14, no. 1, pp. 130–133, Jan. 2024, doi: 10.1109/TTHZ.2023.3327587.

[25] O. Glubokov, X. Zhao, J. Campion, B. Beuerle, U. Shah, and J. Oberhammer, "Investigation of fabrication accuracy and repeatability of high-Q silicon-micromachined narrowband sub-THz waveguide filters," *IEEE Trans. Microw. Theory Techn.*, vol. 67, no. 9, pp. 3696–3706, Sep. 2019, doi: 10.1109/TMTT.2019.2926244.

[26] G. M. Rebeiz and J. B. Muldavin, "RF MEMS switches and switch circuits," *IEEE Microw. Mag.*, vol. 2, no. 4, pp. 59–71, Dec. 2001, doi: 10.1109/6668.969936.

[27] J. Papapolymerou, K. L. Lange, C. L. Goldsmith, A. Malczewski, and J. Kleber, "Reconfigurable double-stub tuners using MEMS switches for intelligent RF front-ends," *IEEE Trans. Microw. Theory Techn.*, vol. 51, no. 1, pp. 271–278, Jan. 2003, doi: 10.1109/TMTT.2002.806513.

[28] S. van Berkel, S. Rahiminejad, R. Lin, and G. Chattopadhyay, "A 250–310 GHz piezo-motor actuated SPDT waveguide switch with high isolation," *IEEE Trans. THz Sci. Technol.*, vol. 13, no. 2, pp. 158–166, Mar. 2023, doi: 10.1109/TTHZ.2022.3221303.

[29] A. J. Alazemi, D. Zarifi, and A. Farahbakhsh, "A broadband contactless gap waveguide microwave switch for X- and Ku-bands applications," *AEU Int. J. Electron. Commun.*, vol. 139, Sep. 2021, Art. no. 153929, doi: 10.1016/j.aeue.2021.153929.

[30] J. Campion, U. Shah, and J. Oberhammer, "Elliptical alignment holes enabling accurate direct assembly of micro-chips to standard waveguide flanges at sub-THz frequencies," in *IEEE MTT-S Int. Microw. Symp. Dig.*, Jun. 2017, pp. 1262–1265, doi: 10.1109/MWSYM.2017.8058838.

[31] Z. Baghchehsaraei, U. Shah, J. Åberg, G. Stemme, and J. Oberhammer, "MEMS reconfigurable millimeter-wave surface for V-band rectangular-waveguide switch," *Int. J. Microw. Wireless Technol.*, vol. 5, no. 3, pp. 341–349, Jun. 2013, doi: 10.1017/s1759078713000378.

[32] N. Vahabisani and M. Daneshmand, "Monolithic millimeter-wave MEMS waveguide switch," *IEEE Trans. Microw. Theory Techn.*, vol. 63, no. 2, pp. 340–351, Feb. 2015, doi: 10.1109/TMTT.2014.2378253.

[33] N. Zhang, R. Song, J. Liu, and J. Yang, "A packaged THz shunt RF MEMS switch with low insertion loss," *IEEE Sensors J.*, vol. 21, no. 21, pp. 23826–23837, Nov. 2021, doi: 10.1109/JSEN.2021.3113647.

[34] D. Laemmle, H. F. Schlaak, C. Weickhmann, and R. Jakoby, "Proof of concept for a WR-2.2 MEMS waveguide switch," in *Proc. 41st Int. Conf. Infr., Millim., THz Waves (IRMMW-THz)*, Sep. 2016, pp. 1–2, doi: 10.1109/IRMMW-THz.2016.7758655.

[35] T. Reck, C. Jung-Kubiak, and G. Chattopadhyay, "A 460 GHz MEMS-based single-pole double-throw waveguide switch," in *IEEE MTT-S Int. Microw. Symp. Dig.*, Jun. 2018, pp. 773–775, doi: 10.1109/MWSYM.2018.8439196.

[36] T. Reck, C. Jung-Kubiak, and G. Chattopadhyay, "A 700-GHz MEMS waveguide switch," *IEEE Trans. THz Sci. Technol.*, vol. 6, no. 4, pp. 641–643, Jul. 2016, doi: 10.1109/TTHZ.2016.2574304.

[37] S. Rahiminejad, S. Van Berkel, R. H. Lin, C. Jung-Kubiak, G. Chattopadhyay, and M. Rais-Zadeh, "A MEMS contactless rotating terahertz waveguide switch," in *Proc. IEEE 35th Int. Conf. Micro Electro Mech. Syst. Conf. (MEMS)*, Jan. 2022, pp. 223–226, doi: 10.1109/MEMS51670.2022.9699786.

[38] Y. Feng and N. S. Barker, "High performance 500–750 GHz RF MEMS switch," in *IEEE MTT-S Int. Microw. Symp. Dig.*, Jun. 2017, pp. 1095–1097, doi: 10.1109/MWSYM.2017.8058786.

[39] W.-C. Lai, C.-C. Chou, S.-C. Huang, T.-H. Huang, and H.-R. Chuang, "75–110-GHz *W*-band high-linearity traveling-wave T/R switch by using negative gate/body-biasing in 90-nm CMOS," *IEEE Microw. Wireless Compon. Lett.*, vol. 27, no. 5, pp. 488–490, May 2017, doi: 10.1109/LMWC.2017.2690837.

[40] F. Meng, K. Ma, K. S. Yeo, and S. Xu, "Monolithic sub-terahertz SPDT switches with low insertion loss and enhanced isolation," *IEEE Trans. THz Sci. Technol.*, vol. 8, no. 2, pp. 192–200, Mar. 2018, doi: 10.1109/TTHZ.2017.2786024.

[41] M. Uzunkol and G. M. Rebeiz, "140–220 GHz SPST and SPDT switches in 45 nm CMOS SOI," *IEEE Microw. Wireless Compon. Lett.*, vol. 22, no. 8, pp. 412–414, Aug. 2012, doi: 10.1109/LMWC.2012.2206017.

Armin Karimi (Graduate Student Member, IEEE) was born in Kermanshah, Iran, in 1993. He received the B.Sc. degree in electrical engineering, focusing on communication systems and the M.Sc. degree in applied electromagnetics, fields, and waves from the University of Tehran, Tehran, Iran, in 2016 and 2019, respectively. He is currently pursuing the Ph.D. degree in silicon micromachined terahertz and subterahertz components and systems with the Division of Micro and Nano Systems, KTH Royal Institute of Technology, Stockholm, Sweden.

His research interests are applied electromagnetics, RF-MEMS, nanofabrication, microwave and mm-wave active and passive components, array antenna, filter, imaging systems, metamaterial and metasurface, and signal chain design.

Mr. Karimi was a recipient of the Young Engineer Award at European Microwave Week 2023, Berlin, Germany, and the Best Student Paper Award presented at Swedish Microwave Days 2023, Stockholm.
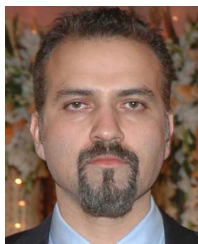
Umer Shah (Senior Member, IEEE) was born in Pakistan, in 1981. He received the B.S. degree in engineering from the GIK Institute Pakistan, Khyber Pakhtunkhwa, Pakistan, in 2003, the Master of Science degree in wireless engineering from the Technical University of Denmark (DTU), Kongens Lyngby, Denmark, in 2007, and the Ph.D. degree in microsystem technology from the KTH Royal Institute of Technology, Stockholm, Sweden, in 2014.

Since May 2014, he has been a Post-Doctoral Researcher at the Micro and Nano Systems Group, KTH Royal Institute of Technology. He has authored and coauthored more than 30 reviewed research papers. His research focus includes RF MEMS-based filters, phase shifters, and matching circuits and antennas.

Dr. Shah is a recipient of the Best Student Paper Award presented at Asia Pacific Microwave Conference 2010, Yokohama, Japan, and the "2014 IEEE MTT Graduate Fellowship Award" for his research activities.

Suxian Yu (Student Member, IEEE) was born in Jilin, China, in 1992. She received the B.Sc. and M.Sc. degrees in mechanical and electrical engineering from Beijing Institute of Technology, Beijing, China, in 2013 and 2016, respectively. She is currently pursuing the Ph.D. degree in micromachined sub-THz reconfigurable circuits with the Division of Micro and Nano Systems, KTH Royal Institute of Technology, Stockholm, Sweden.

Her current research interest is millimeter and submillimeter calibration switch circuits for space applications.

Joachim Oberhammer (Senior Member, IEEE) was born in Brunico, Italy, in 1976. He received the M.Sc. degree in electrical engineering from Graz University of Technology, Graz, Austria, in 2000, and the Ph.D. degree in novel RF MEMS switch and packaging concepts from the KTH Royal Institute of Technology, Stockholm, Sweden, in 2004.

He was a Post-Doctoral Research Fellow with Nanyang Technological University, Singapore, in 2004, and Kyoto University, Kyoto, Japan, in 2008. He was leading radio frequency/microwave/terahertz (THz) microelectromechanical systems research at the KTH Royal Institute of Technology, until 2010, and an Associate Professor, until 2015. He is currently a Professor of microwave and THz microsystems. He was a Guest Researcher with Nanyang Technological University, in 2007, and the NASA Jet Propulsion Laboratory, Pasadena, CA, USA, in 2014. He has authored or coauthored more than 100 reviewed research articles. He holds four patents.

Dr. Oberhammer has been a Steering Group Member of the IEEE MTT-S and the AP-S Chapters Sweden, since 2009. He served as a TPRC Member for the IEEE Transducers in 2009 and 2015, the IEEE International Microwave Symposiums from 2010 to 2016, the IEEE Micro Electromechanical Systems in 2011 and 2012, and the IEEE Radio and Wireless Week in 2015 and 2016. Since 2014, he has been a Steering Group Member of the Young Academy of Sweden. He was a recipient of the Award by the Ericsson Research Foundation, a grant by the Swedish Innovation Bridge, and a scholarship by Japanese Society for the Promotion of Science, in 2004, 2007, and 2008, respectively. The research work he has been heading received six best paper Awards (five of which at IEEE conferences) and four IEEE Graduate Fellowship Awards (by the IEEE MTT-S and by AP-S), since 2009. In 2013, he received an ERC Consolidator Grant from the European Research Council.